

# Imaging and Calibration of Electromagnetic Inversion Data With a Single Data Set

EUNGJOO KIM<sup>1</sup>, CENA T. MOHAMMADI<sup>1</sup>, MOHAMMAD ASEFI<sup>2</sup>, JOE LOVETRI<sup>1</sup> (Senior Member, IEEE), IAN JEFFREY<sup>1</sup> (Member, IEEE), AND COLIN GILMORE<sup>1</sup> (Senior Member, IEEE)

<sup>1</sup>Department of Electrical and Computer Engineering, University of Manitoba, Winnipeg, MB R3T 2N2, Canada

<sup>2</sup>AGCO Corporation, Winnipeg, MB R3T 6A8, Canada

CORRESPONDING AUTHOR: C. GILMORE (e-mail: colin.gilmore@umanitoba.ca)

This work was supported in part by the Natural Sciences and Engineering Research Council of Canada; in part by the Canada Research Chair Program; in part by MITACS Canada; and in part by AGCO Corporation.

**ABSTRACT** Electromagnetic Imaging (EMI) systems use a large number of co-resident antennas usually connected to a Vector Network Analyzer via a switch. A numerical model is used to model the physical electromagnetic problem and an inversion algorithm is used to invert the collected data to produce an image of the target. However, before the computer model can be used, the raw VNA measurements must be calibrated to bridge the computational model and the true system physics. Traditional calibration approaches usually require two data sets: a data set measured from a known target for calibration purposes and a data set measured for the unknown target. In this paper, we introduce a new calibration method to calibrate and image using a single S-parameter measurement of the unknown target only. We apply this method to EMI inside of grain bins. This proposed calibration workflow: (1) estimates the bulk contents of the grain bin using a parametric inversion and (2) uses the bulk results to subsequently estimate per-channel calibration coefficients for both the transmit and receive paths to each antenna. The novel calibration procedure is demonstrated via both synthetic and experimental results, showing that single-data set calibration can provide similar quality results as traditional two-data set calibration.

**INDEX TERMS** Inverse problems, calibration, microwave tomography, inverse imaging.

## I. INTRODUCTION

**M**OST of the world's crops are harvested then stored for later processing and consumption. When in storage, the moisture and temperature of the crop are important factors when storing grain and in general, high moisture and/or high temperature levels within the bulk of the grain can result in grain spoilage. Previous research has shown that grain's moisture and temperature directly effect the complex permittivity of the grain [1], which allows the monitoring of stored grain via Electromagnetic Inversion (EMI). Grain-bin EMI allows the reconstruction of 3D maps of the permittivity inside the bin which can be used to monitor the grain for safe storage conditions over time. Results for such systems have been previously reported in [2], [3], [4], [5].

A simplified grain-bin EMI system is illustrated in Fig. 1. Signals are generated and S-parameters are measured using Vector Network Analyzer (VNA), then delivered through a switch network and coaxial cables to 24 antennas installed inside a bin. These S-parameter measurements at

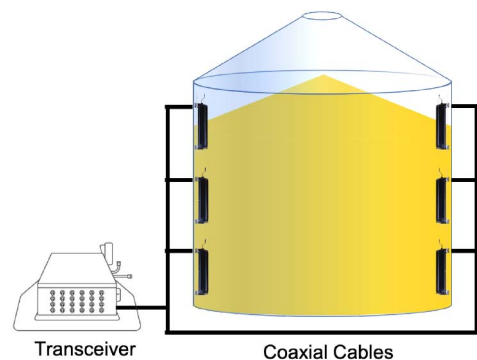


**FIGURE 1.** A simplified schematic of the Electromagnetic Inverse (EMI) system showing only 6 antennas. 24 antennas are supported in the industrial system.

a set of specific frequencies are then calibrated and used in an inversion algorithm that provides quantitative 3D images of the complex electric permittivity of the content

of the bin. This two-data set process is the same for many other types of inversion algorithm and applications (e.g., [6], [7], [8], [9], [10], [11] and others).

The contribution of this paper involves the calibration step in the inversion process. There are many reasons that calibration is required, the foremost being that the inversion codes assume knowledge of electromagnetic fields at a point, but the VNA measures a ratio of voltages at a port. Additionally, difference between the computer model and the physical system interfere with accurate inversion, and further, the switch, cables, and antennas all have imperfections that must be compensated for before inversion. That is, the S-parameters are distorted due to the presence of the measurement system. Calibration attempts to account for and/or remove the effects of the system on the measurements.

Typically we attempt to calibrate an EMI system using a measurement of a known target (or material state). Calibration coefficients can then be generated to compensate for each channel by comparing the measurement with the synthetic scattering of the known target. However, in grain bins the ability to put a known target in the bin is limited or impossible. We refer to imaging systems where we cannot introduce a calibration target as *uncooperative*. The goal of the technique described in this manuscript is to eliminate the need for the known target and effectively extract the calibration data from every data set acquired from any unknown target.

The reason we seek this new calibration technique is that it is capable of detecting regions of concern within a stored grain mass before the grain starts to spoil. While the process of stored grain spoiling always leads to higher permittivity which can be readily detected by the differential calibration method, it is common for grain handlers to place grain of different moisture contents and temperatures inside of bins (particularly larger bins). This sometimes involves putting grain in a bin that is near spoiling. At this time, grain handlers can turn on fans or move the grain if it starts to spoil (i.e., they can take action to prevent the regions of concern from spoiling). It is thus useful for handlers to know the exact regions to monitor from the moment they load the bin.

## II. TWO-DATA SETS: CALIBRATION AND IMAGING

We first describe the traditional calibration procedure used for EMI systems. Applied to grain bin imaging systems the traditional calibration process is outlined in Fig. 2. The calibration and imaging process requires two S-parameter measurements of each possible transmit/receive pair, which we denote  $S_{xy}$ .<sup>1</sup> Examples of inversion systems that use this technique are discussed in [7], [12], [13], [14]. S-parameters are measured from the antenna pairs of receivers  $x$  and transmitters  $y$  at time  $t_1$  when the state inside the imaging chamber is known. Examples of known targets used to calibrate an

1. In a 24 antenna system,  $x$  and  $y$  vary over 1 to 24, resulting in a  $24 \times 24$  S-parameter matrix. The diagonal elements are usually ignored, resulting in  $24 \times 23$  data points.

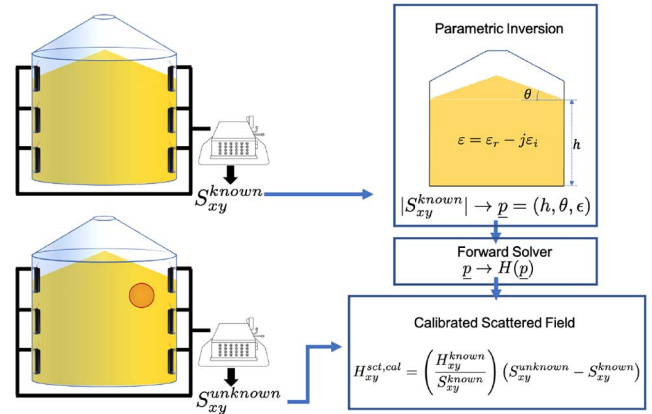


**FIGURE 2.** The previously existing inversion workflow reconstructs a parametric homogeneous model of a known configuration (top). The fields from the parametric model are given to a calculation where subsequent measurements are calibrated (bottom). This process requires two data sets taken with different materials states in the bin.

EMI system include metallic targets [12], or commonly, a measurement without any target present at all [7]. Regardless of the type of known target, we refer to these measurements as  $S_{xy}^{known}$ . The key point is that the fields from this target can be computed using the computational model of the system. Within this work, we refer to the fields generated by our computational model (including the known target) as  $H_{xy}^{known}$ . We have chosen  $H$  to refer to the simulated fields as antennas inside the grain bin measure the tangential magnetic field on the metallic bin wall [15]. Measurements associated with an unknown target of interest (e.g., an unknown state of grain) are referred to as  $S_{xy}^{unknown}$ . Using the two S-parameter measurements and the computed fields for the known state, calibrated scattered fields,  $H_{xy}^{sct.cal}$  for the unknown object are calculated according to:

$$H_{xy}^{sct.cal} = \left( \frac{H_{xy}^{known}}{S_{xy}^{known}} \right) (S_{xy}^{unknown} - S_{xy}^{known}) \quad (1)$$

where we emphasize that for this calculation, both S-parameters and fields are in linear (not dB) form.

This standard calibration procedure removes system errors that are caused by the difference between the actual system and the simulated model. Another way of considering this method is that each possible transmit/receive antenna pair ( $24 \times 23$  data points) has an individual compensation coefficient that converts the S-parameter to fields ready to be used in an inversion algorithm.

### A. TWO DATA SET CALIBRATION AND IMAGING IN GRAIN BINS

Our proposed calibration process builds on a previously presented two-step inversion process presented in [5]. In this section we describe this pre-existing inversion workflow in grain bins. The key step in applying this workflow to grain bins is the addition of the ‘Parametric Inversion’ in Fig. 2. With a lab-based (cooperative) imaging system, we

can introduce known calibration targets at will. In an uncooperative imaging system such as the grain bin, we cannot introduce a known target. It is important to note that successful imaging often requires the known calibration state to be similar to the unknown target. For this reason it is generally not possible to use the empty bin as a known state for successful calibration of other bin states, and we must have a way of determining an approximate state of the grain from the raw  $S$ -parameter data.

Similar to other works [16], [17], our existing approach is a 2-step inversion process that generates an simple initial material model first, which is used in later full inversions. Referring to Fig. 2, this workflow is:

- 1) Collect  $S$ -parameter data,  $S_{xy}^{known}$  from the system when the bin has no suspected hot-spot. Using raw, uncalibrated data, obtain the parametric model, which subsequently becomes our known calibration model (see Section II-B for details).
- 2) Using the parametric model, call a forward solver and generate the fields for the known state,  $H_{xy}^{known}$ .
- 3) Take a second data set at a later time,  $S_{xy}^{unknown}$ , when there may be a hot-spot in the bin.
- 4) Use (1) to calibrate the fields.
- 5) Send the calibrated fields to the 3D FEM-CSI inversion algorithm, using the parametric model as the background materials.

### B. PARAMETRIC INVERSION DETAILS

Our parametric model of the bin contents consists of a bulk average complex-value permittivity  $\epsilon = \epsilon_r - j\epsilon_i$ , the grain's height at the bin wall,  $h$ , and angle of repose of the grain (cone angle)  $\theta$ . These four parameters  $\underline{p} = (h, \theta, \epsilon)$  are obtained using a phaseless parametric inversion [5], where we use only the magnitudes of the measured  $S$ -parameters to obtain the 4 parameters. Since there are only 4 parameters that describe the entire contents of the bin, parametric inversion works well with uncalibrated, raw measurements. We assume a simple scaling factor to change from  $|S|$  to  $|H|$  as the measurement system and simulation are always scaled somewhat differently (e.g.,  $S$ -parameters are actually measuring a ratio of voltages while the computational model uses fields). We thus determine  $\underline{p}$ 's in experimental bins by minimizing the following objective function:

$$\underline{p} = \underset{\tilde{\underline{p}}}{\operatorname{argmin}} \sum_{x,y} \left\| \left| \alpha_x(\tilde{\underline{p}}) S_{xy}^{unknown} \right| - \left| H_{xy}(\tilde{\underline{p}}) \right| \right\|_2^2 \quad (2)$$

where  $\alpha_x$  is a per-transmitter factor used to scale the average signal levels between the forward-solver-generated estimate fields  $H_{xy}(\underline{p})$  and the VNA measurements  $S_{xy}^{unknown}$ , given by:

$$\alpha_x(\underline{p}) = \frac{\sum_y |H_{xy}(\underline{p})|}{\sum_y |S_{xy}^{unknown}|}. \quad (3)$$

This cost function is constructed using phaseless data and minimized using the Nelder-Mead simplex optimization

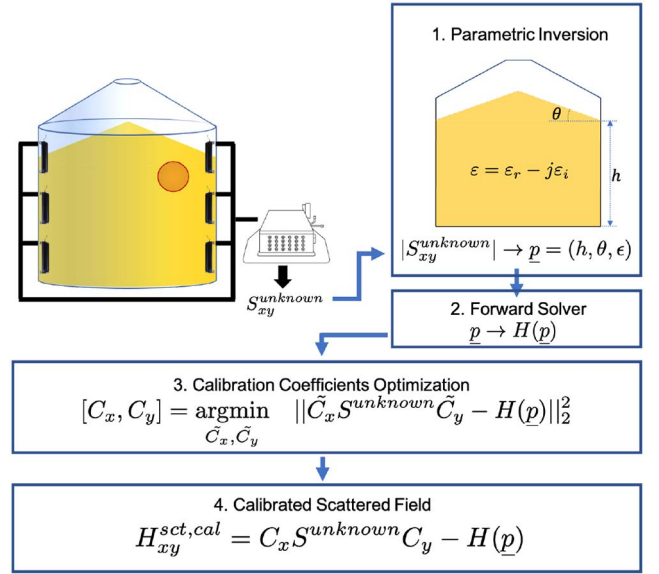


**FIGURE 3.** The proposed single-shot calibration method consists of 4 steps: 1) phaseless parametric inversion optimizes on parameter  $\underline{p}$  with a single  $S$ -parameter measurement, 2) a forward model is created with  $\underline{p}$ , 3) channel-specific calibration coefficients are determined through optimization, and 4) the parametric model and calibration coefficients are used to produce calibrated scattered-fields.

method [5]. Once solved,  $\underline{p}$  provides both a bulk estimate of the grain inside the bin as well as a calibration model for further inversion. Once extracted,  $\underline{p}$  is used to construct a forward model that solves for  $H_{\underline{p}}$ , which are the fields associated with that set of materials in the bin.

It is important to note that inhomogeneities may be present in the bin that cannot be modelled with such a simple parametric model  $\underline{p}$ . Such inhomogeneities result in a higher residual objective function after optimization, and it is these residuals that form the basis of the scattered fields that we subsequently invert to improve the permittivity model.

### III. SINGLE DATA SET CALIBRATION

Herein, we propose a method to calibrate with a single set of  $S_{x,y}$  measurements. We called this procedure “single data set” or “single-shot” calibration [18].<sup>2</sup> After the calibration process, a full 3D inversion is run on the calibrated data; the work-flow is outlined in Fig. 3, and consists of 4 steps:

- 1) Same as the traditional process, collect a single set of  $S$ -parameter data, but this time we refer to it as  $S_{xy}^{unknown}$ .
- 2) Run the parametric inversion algorithm on this data set and run a forward solver on the parameters, thus generating  $H(\underline{p})$ .
- 3) Perform a non-linear optimization to obtain per-channel calibration coefficients (see below for full description).
- 4) Using the per-channel calibration coefficients, calibrate the data and send these scattered field data to the full 3D inversion algorithm.

2. The core idea of this algorithm was previously presented in [18], but only for a single set of coefficients on simulated data.

This process allows one to generate the parametric model, calibrate, and perform a full inversion on a single data set, and is described in more detail below.

### A. SINGLE DATA SET CALIBRATION AND GENERATION OF SCATTERED FIELDS

Our proposed single-shot calibration uses  $S_{xy}^{unknown}$  and  $H_{xy}^{known}$  data to obtain a set of restricted calibration coefficients (step 3 above). The key to this step of our proposed method is that we have only one calibration coefficient per transmit or receive channel (for a total of 48 coefficients in our case). Per-channel coefficients are motivated by the assumption that each transmit/receive channel can be treated as a linear system that modifies the transmitted signal only by modifying the magnitude and phase of the signal (and is independent for every channel). We use a different set of coefficients for transmit and receive mode because signals pass through different paths within the switch depending on whether the switch is in transmit or receive mode (put another way, the switch is not a reciprocal network). We represent these per-channel calibration coefficients as diagonal matrices:

$$C_x = \begin{bmatrix} c_{x1} & & \\ & \ddots & \\ & & c_{xN} \end{bmatrix}, C_y = \begin{bmatrix} c_{y1} & & \\ & \ddots & \\ & & c_{yN} \end{bmatrix}, \quad (4)$$

where  $N$  is the total number of antennas (i.e., transmit/receive channels) and  $c_{xj}$  is the complex calibration coefficient for receive path  $j$ ,  $j = 1, 2, \dots, N$ , and  $c_{yj}$  is the transmit path. These are used to capture the phase shift and channel loss of the signal pathway.

We obtain estimates of these calibration coefficients,  $C = [C_x, C_y]$ , by minimizing the following objective function:

$$C = \underset{\tilde{C}}{\operatorname{argmin}} \quad \|\tilde{C}_x S^{unknown} \tilde{C}_y - H(\underline{p})\|_2^2, \quad (5)$$

where  $S^{unknown}$  are the raw measurements, and  $H(\underline{p})$  are the total fields at the receive points obtained from the parametric inversion (step 1). The  $C$  matrices are diagonal, and e.g., the result of  $c_{x2} S_{2,1} c_{y1}$  thus represents the calibrated field from receive channel 2 and transmit channel 1.

Based on the diagonal structure of the  $C$  matrices we have  $(C S^{unknown} C)_{xy} = c_x S_{xy}^{unknown} c_y$  which clearly shows that the coefficients  $c_x$  and  $c_y$  act to account for cable loss and phase shifts along the channels  $x$  and  $y$  in the measurement path that are not accounted for in the forward model used to generate  $H(\underline{p})$ .

The justification of our per-channel calibration model is that the main component of the signal deterioration is simply a magnitude and phase shift in each transmit/receive channel in the measurement system. A full calibration would require a calibration matrix the same size as the  $S$  matrix, rather than a diagonal matrix. Our use of diagonal  $C$  matrices means that cross-channel signal leakage is currently being ignored in our proposed calibration method. However, the problem

of this leakage is minimized by design in the switch where the majority of leakage occurs. Another way of viewing our use of diagonal calibration matrices is that each channel is considered to be a lossy transmission line (not a full-port device between the VNA and the antennas). The coefficient  $C$ -matrix also accounts for the antenna factor (that compensates for the change between the field and voltage ratio measurements).

Once matrices of per-channel calibration coefficients for both signal paths are determined by optimizing (5), the calibrated scattered field data  $H_{xy}^{sct,cal}$  are calculated as:

$$H_{xy}^{sct,cal} = C_x S^{unknown} C_y - H(\underline{p}). \quad (6)$$

That is, the bulk parametric inversion  $\underline{p}$  serves not only to provide an approximate known state for calibration via (5), but also serves as the background medium used to define the scattered fields for subsequent inversion. The calibrated scattered fields,  $H_{xy}^{sct,cal}$  can now be sent to the inversion algorithm.

### IV. INVERSION METHOD

Once  $H^{sct,cal}$  is produced by the single-shot calibration process, we can proceed to apply an inversion algorithm to detect hot-spots that may be present in the grain. This is accomplished using a parallel 3D Finite-Element Contrast Source Inversion Method (FEM-CSI) algorithm. Details of the basic FEM-CSI algorithm are discussed in [19], and its application to the grain bin problem is presented in [2], [3], [4].

### V. SYNTHETIC RESULTS

To show the effectiveness of the proposed single-shot calibration method, we first consider a synthetic analysis with bin dimensions and frequencies chosen to mimic an experimental system. The bin features a flat-bottomed bin with a wall height of 25.75 m and a diameter of 23.64 m. Twenty four (24) antennas are installed on the interior of the bin wall, placed at 12 different radial locations in pairs (similar to the hour indicators marked on a clock). Antenna heights are selected to maximize the number of possible antennas heights given the restrictions of bin construction (i.e., antennas must avoid the bolts that hold the bin together). A simple schematic of the synthetic bin is illustrated in Fig. 4. A frequency of 17 MHz was selected for this experiment (a wavelength of 17.6 m in free space). The parameters of the simple grain model are given as  $h = -4.0$  m,  $\theta = 15^\circ$ , and  $\epsilon_{rel} = 4.1 - j0.48$ . A spherical hot-spot is submerged in the grain. The hot-spot's permittivity is  $7 - j0.8$  and its diameter is 3 m (or  $\approx 1/6$  of a wavelength in free space). The total fields  $H^{tot}$  of this synthetic configuration were then generated with a full-3D FEM based forward direct solver [19].

Next, simulated per-channel shifts were added through per-channel magnitude and phase shifts to create synthetic measurement system errors:  $S^{unknown} = (C_x^{synth})^{-1} H^{tot} (C_y^{synth})^{-1}$ , where  $C_x^{synth}$  and  $C_y^{synth}$  were created based on estimates of

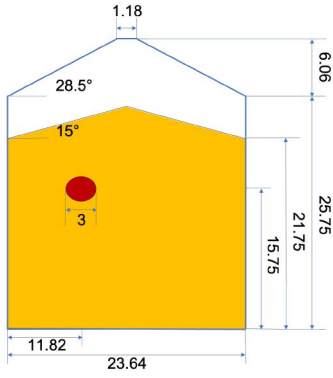
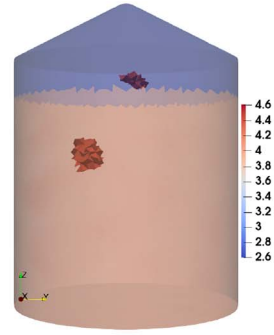
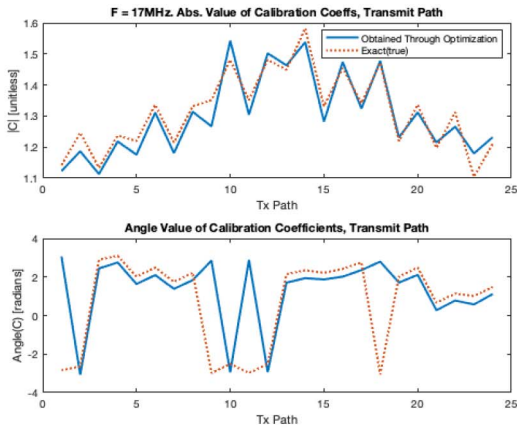


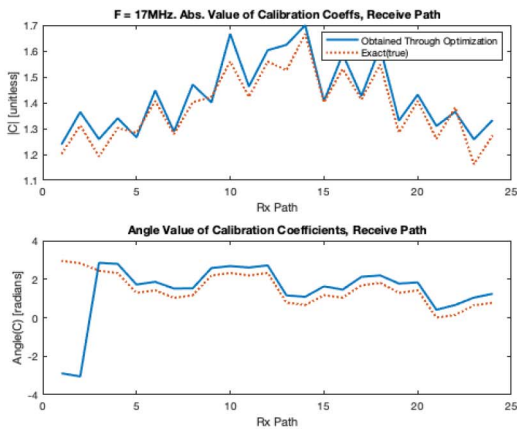
**FIGURE 4.** Layout of flat-bottom style grain bin for synthetic test. The permittivity of the grain is  $4.1 - j0.48$  while the permittivity of the hot-spot is  $7 - j0.8$ .



(a) Single-shot Calibrated Image (synthetic data)



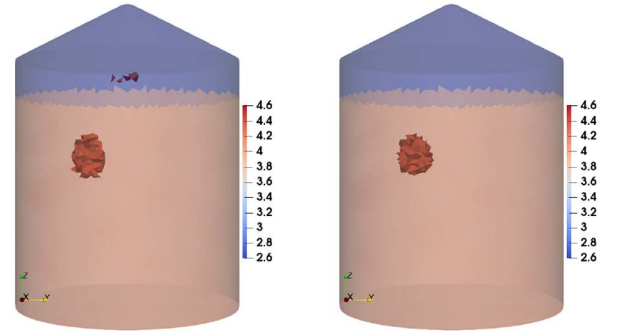
(a)



(b)

**FIGURE 5.** Calibration coefficients used for the synthetic analysis. (a) Calibration coefficients per transmit channel. (b) Calibration coefficients per receive channel. The exact coefficients used to manipulate the synthetic data are shown in red, the estimated coefficients computed from optimization are shown in blue.

cable phase shifts and losses from the experimental system installed on the bin on which this synthetic experiment was modelled. These data,  $S^{known}$ , provide the initial input to our proposed single-shot calibration method. The magnitude and phase of the true transmit/receive coefficients  $C_x^{synth}$  and  $C_y^{synth}$  are shown in Fig. 5.



(b) Image with No Measurement Error (parametric background) (c) Image with No Measurement Error (incident background)

**FIGURE 6.** FEM-CSI inversion 3D image of  $\Re(\epsilon)$  with a threshold. (a) The outcome of the single-shot calibration procedure on synthetic data manipulated with per-channel magnitude and phase shift. (b) Ideal results without measurement error using the same parametric background. (c) Ideal results without measurement error using the perfect background. All tetrahedrons beyond a threshold of 4.4 are solid. The one-shot calibrated image compares favorably with the ideal image.

Step 1 of the proposed method is to obtain the material parameters  $\underline{p}$  of the estimated background model via phaseless parametric inversion. We note that the hot-spot cannot be represented by the parametric model as the permittivity of this model is expected to be homogeneous, but the fields caused from the hot-spot are present in the simulated S-parameter measurements. The inverted parameters were obtained as  $\epsilon_{rel} = 4.09 - j0.47$ ,  $h = -3.89$  m and  $\theta = 12.31^\circ$  and matched well when compared to the true values.  $H(\underline{p})$  was generated using these parameters.

Moving on to Step 2 of the proposed calibration scheme we next solved (5), using the non-linear optimization tool provided in MATLAB. This procedure produces estimates of the Tx/Rx coefficients of  $C_x^{synth}$  and  $C_y^{synth}$ . The estimated coefficients  $C$  after the optimization are shown in Fig. 5. These optimization-generated coefficients are quite close to the true values, but not exact. The complex percent relative  $L_2$ -norm of the true vs estimated are 15.2% for the transmit path and 19.0% for the receive path coefficients. We do not expect exact values as the fields from the hot spot, and errors in the phaseless parametric optimization (i.e., errors in our parameters  $\underline{p}$ ), mean

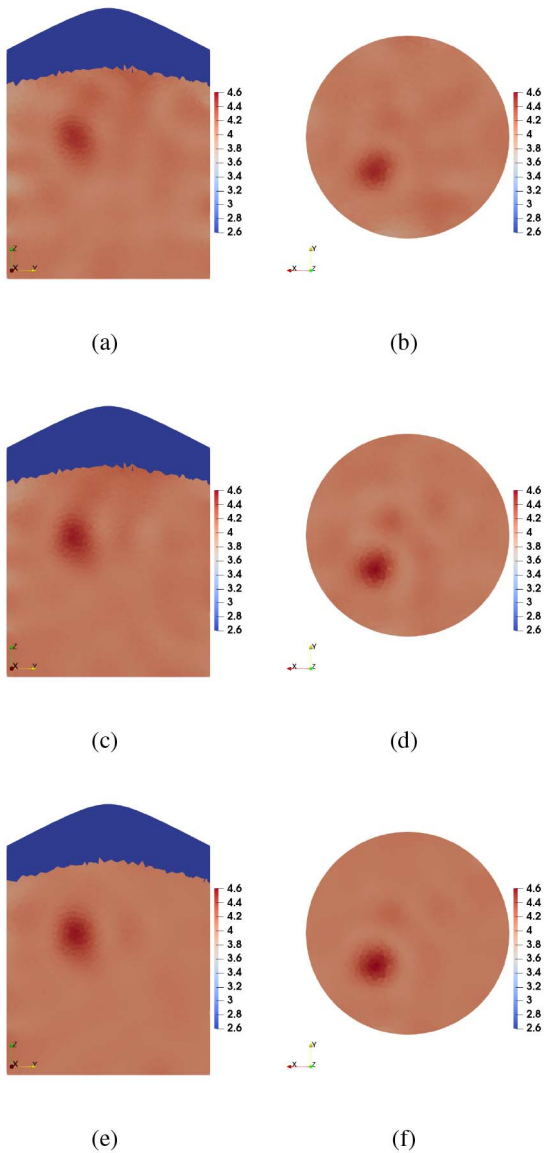


**FIGURE 7.** Further 2D slices of the FEM-CSI result for the synthetic single-shot calibration. (a) Vertical slice and (b) horizontal slice of the one-shot calibrated data inversion. (c) Vertical slice and (d) horizontal slice of the ‘ideal’ data inversion with the same parametric background. (e) Vertical slice and (f) horizontal slice of the ‘ideal’ data inversion with the perfect background.

we cannot obtain an exact fit for the  $C$  matrices. While there is clearly some error between the true and estimated  $C$ 's, the ultimate determination whether the estimated values are accurate enough is in the generation of the inverted images based on these estimated  $C$ 's. We turn to those images next.

The calibrated scattered fields are obtained following (6) and are given to the FEM-CSI algorithm. The inversion results using the proposed single-shot calibration are shown in Fig. 6 (a), and Fig. 7 (a)–(b).

The benefit of our synthetic example is that images can also be generated for the case without cable coefficients. Specifically, we create a near “ideal” image using the

following data:

$$H^{sct,ideal} = H^{tot} - H(p). \quad (7)$$

$H^{sct,ideal}$  is the ideal scattered field data and the data do not include errors in the measurement system (but note that they still include the imperfect parametric-obtained background field). A more accurate image could be obtained by utilizing the perfect background information (i.e., use the homogeneous grain bulk without the hot-spot region). However, this perfect prior information is not accessible for actual bins, so we have instead used the available parametric-generated prior information. The results of the 3D FEM-CSI inversion on these ideal data are shown in Figs. 6 (b) and 7 (c)–(d). The results obtained via the single-shot (proposed) calibration are very similar to the ideal results, demonstrating the potential of the proposed one-shot calibration method.

## VI. EXPERIMENTAL RESULTS

As an experimental test, we applied the one-shot calibration method to a scaled (small) grain bin that was previously reported in [15], [20]. We used the scaled bin as we can perform a controlled experiment: it is feasible to create and control the hot-spot in a homogeneous background of grain (unlike the much larger simulated grain bin). This barrel's schematic diagram and images of the interior of the test barrel are shown in the Fig. 8.

The experimental bin is a cylindrical metal barrel that has a height of 0.81 m and a radius of 0.28 m. The volume of this lab-sized bin is about 190 L (4.5 bushels). 24 antennas are installed inside the grain bin wall in a stair case style in order to spread the antennas out on the bin wall as much as feasible. In order to keep air circulated throughout the grain, a false-bottom floor was welded at a height of 10 cm from the ground, and the lid was placed on top but not tightened. In contrast with previous reports with this system [20], we have added ferrite behind each antenna, which has the main effect of increasing the signal strength. These modified antennas are described in [21], but operate in a very similar manner to previously reported antennas in [20] (with an increase in signal strength).

The antennas are connected to coaxial cables via a switch to transfer data to a VNA.  $S$ -parameter measurements are taken over a range of frequencies from 1 to 1300 MHz. In our experiment, we chose six frequencies from the 240–270 MHz and the 550–570 MHz bands (260, 270, 280, 550, 560, and 570 MHz). We chose the lower band as it is located in the resonance of the antennas [21] and the higher band was chosen to match other frequencies previously used in this scaled grain bin [20]. The wavelength of 250 MHz band is  $\approx 0.70$  m in grain and 550 MHz is  $\approx 0.32$  m in grain.

The barrel was filled with hard red spring wheat and the top surface of the grain was made flat. The grain had a moisture content of 7.5%, which literature values estimate to have a permittivity of approximately  $\epsilon_r = 3 - j0.3$  at

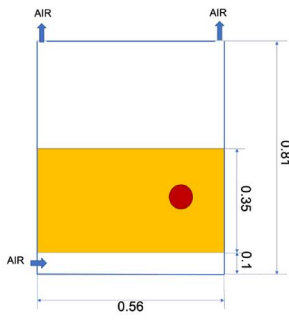
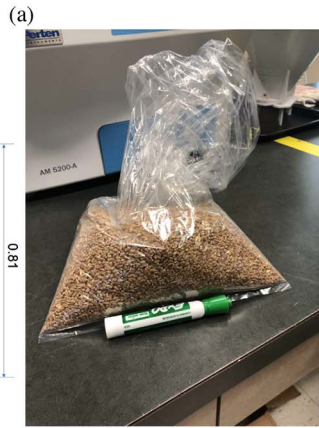


**FIGURE 8.** (a) Exterior photograph of the barrel with the VNA/switch connected to all 24 antennas. (b) Schematic diagram of model grain bin. (c) Image of the wet-grain target with marker for scale. Images of the interior of the barrel are shown in (d) and (e). Grain was filled with a wet grain mixture covered in plastic in a bucket. (d) Dry grain is placed in the bucket then (e) we covered up to the wet grain mixture and leveled the grain.

250 MHz [22].<sup>3</sup> We then collected the first data set of the homogeneous grain:  $S_{xy}^{known}$ .

3. We note that this value of permittivity is quite approximate. The density temperature and particular sub-type of wheat affects the exact value of the permittivity of grain [1]. However, for our purposes the exact expected value is not needed: the bulk permittivity value is obtained from the parametric inversion step.

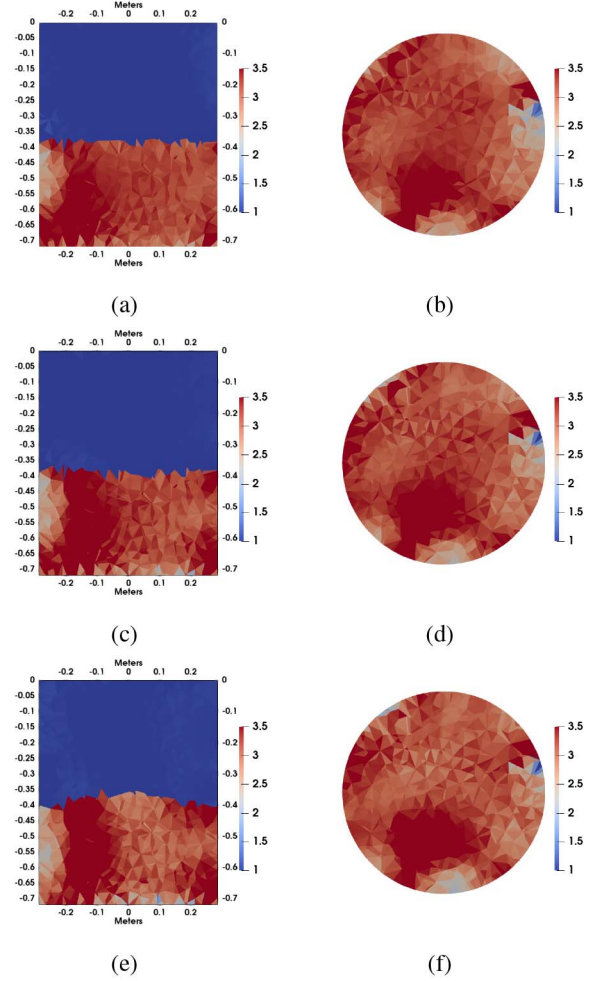


**FIGURE 9.** One-Shot Calibrated Experimental FEM-CSI imaging results of  $Re(\epsilon)$  for the frequency band 200MHz. Standard calibration (a) vertical and (b) horizontal slice at 260MHz, (c) vertical and (d) horizontal slice at 270MHz, and (e) vertical and (f) horizontal slice at 280MHz.

We then created a hot-spot (or target) by adding 210 g of water to 1410 g of grain in a double sealed plastic bag. If all the water had been absorbed, the moisture content of the grain would be 19.5 % (wet basis). If all of this water was to be absorbed by the grain, the approximate permittivity of the grain target would be  $\epsilon_r = 4.5 - j0.6$  [22].<sup>4</sup> The wet-grain target is shown in Fig. 8 (c), and the approximate dimensions were  $8 \times 14 \times 11$  cm. With the help of a plastic pail, we excavated a void the grain and placed the high-permittivity target in the background dry grain. Finally, we filled up the remaining space in the plastic bucket with dry grain to level the grain height. This process simulates, in a

4. Again, this is an estimate. This imaging experiment was performed approximately one hour after mixing the water into the target. Grain can only fully absorb about 2 % moisture per day, so the water was not fully absorbed at the start of the experiment, which means the precise permittivity of the target is not available. However, since the goal of this paper is to compare the traditional calibration with the proposed method, the exact permittivity of the target does not change our conclusions. The important point is that the permittivity is higher than the dry background grain.

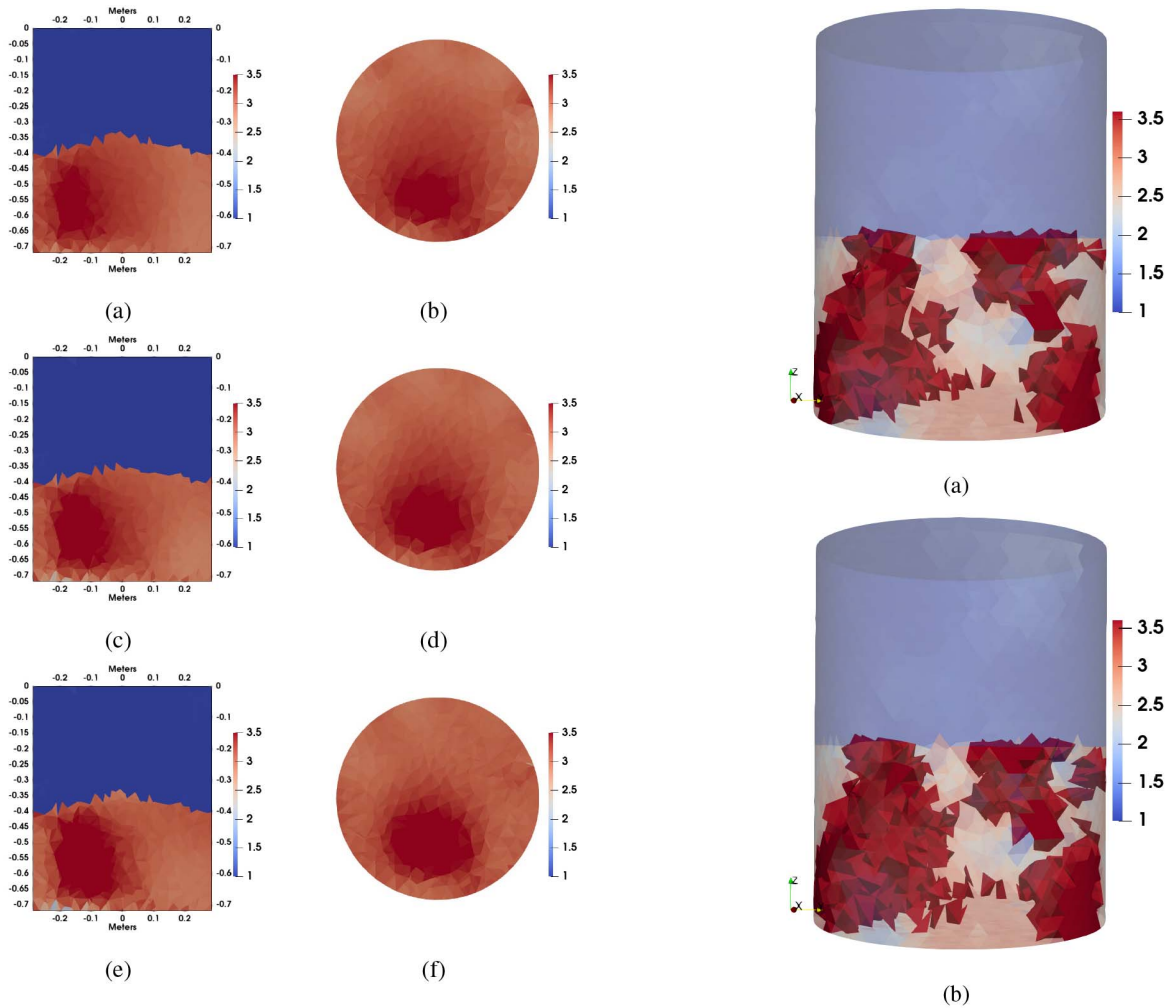


**FIGURE 10.** Traditional Calibrated Experimental FEM-CSI imaging results of  $Re(\epsilon)$  for the frequency band 200MHz. Standard calibration (a) vertical and (b) horizontal slice at 260MHz, (c) vertical and (d) horizontal slice at 270MHz, and (e) vertical and (f) horizontal slice at 280MHz.

**TABLE 1.** Results of parametric inversion for each frequency.

Frequency (MHz)	$\epsilon_{rel}$	Est. Height (from the cave top, meters)	Est. Angle (degree)
260	$3.17 - j0.44$	-0.38	-0.11
270	$3.18 - j0.43$	-0.37	-3.43
280	$3.16 - j0.41$	-0.4	9.74
550	$2.95 - j0.34$	-0.38	0.57
560	$2.93 - j0.35$	-0.38	6.87
570	$2.89 - j0.36$	-0.38	11.4

controlled fashion, how grain typically spoils in bins. Finally, we measured the target data set  $S_{xy}^{unknown}$ .

As with the synthetic example, we used the  $S_{xy}^{unknown}$  measurements in the phaseless parametric inversion algorithm. Parameters after optimization are presented in Table 1. An average permittivity was estimated as  $3.17 - j0.42$  from frequencies in the 250 MHz band, and as  $2.92 - j0.35$  from frequencies in the 550 MHz band. The difference is expected because wheat permittivities are lower at higher frequencies [22]. The estimated angle and the height are

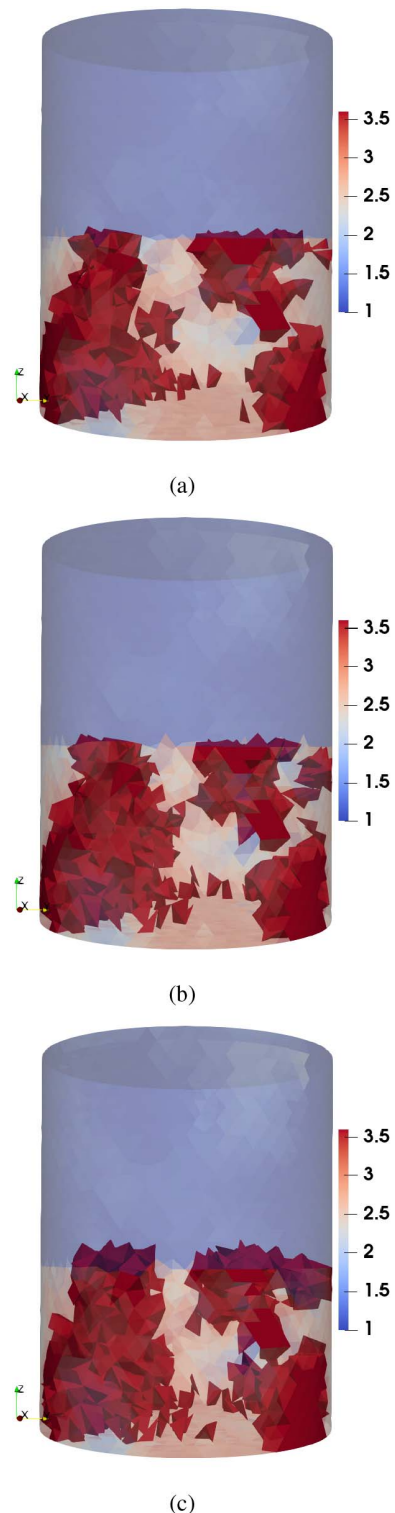


**FIGURE 11.** One-Shot Calibrated Experimental FEM-CSI inversion 3D images of  $Re(\epsilon)$  with a threshold at the frequencies of (a) 260MHz, (b) 270MHz, and (c) 280MHz. All tetrahedrons beyond a threshold of 3.6 are solid.

consistent with the overall frequencies, and have an average of  $4.17^\circ$  and  $-0.38$  m.<sup>5</sup> Next, the homogeneous background

5. There are more errors in the cone angle, which is common as the phaseless parametric inversion algorithm is not as sensitive to cone angle.



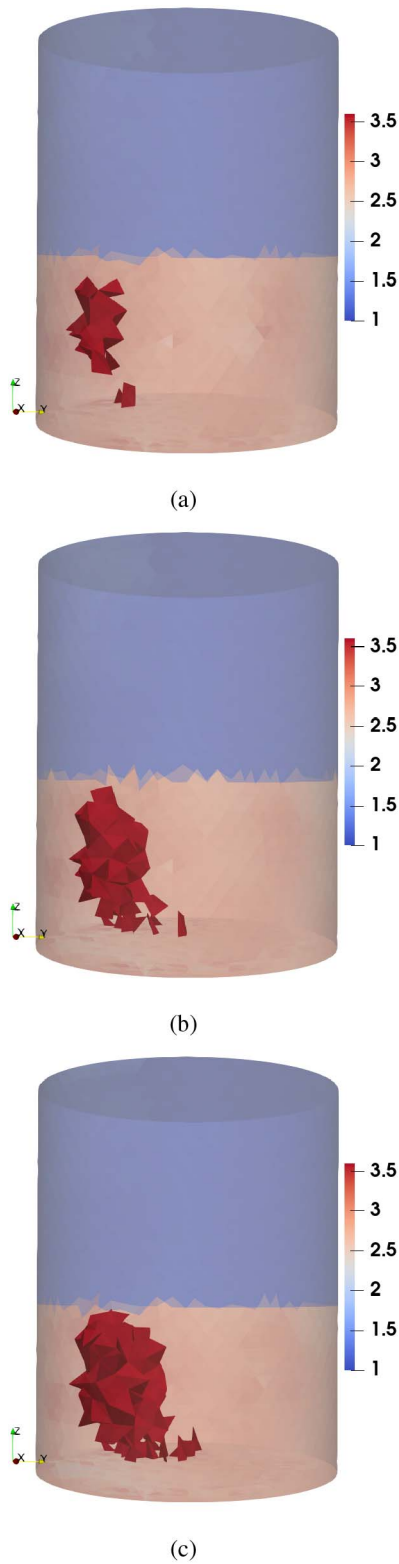


**FIGURE 12.** Traditional Calibrated Experimental FEM-CSI inversion 3D images of  $Re(\epsilon)$  with a threshold at the frequencies of (a) 260MHz, (b) 270MHz, and (c) 280MHz. All tetrahedrons beyond a threshold of 3.6 are solid.

model was generated using those parameters. As explained previously for the synthetic test, the hot-spot cannot be captured from this process.

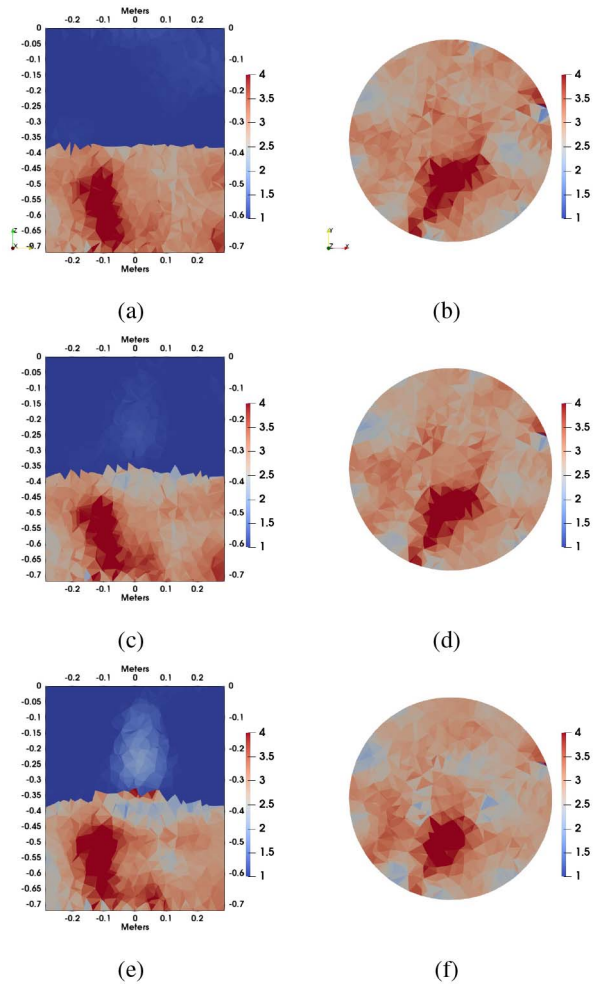


**FIGURE 13.** One-shot Calibrated Experimental FEM-CSI imaging results of  $Re(\epsilon)$  for the frequency band 500MHz. Standard calibration (a) vertical and (b) horizontal slice at 550MHz, (c) vertical and (d) horizontal slice at 560MHz, and (e) vertical and (f) horizontal slice at 570MHz.

The next process is to compute calibration coefficients using the background model  $H(p)$  and raw measurement  $S^{unknown}$ . The calibration objective function of (5) is minimized to be able to capture calibration coefficients in the transmit and receive state. The coefficients that were computed from this process between transmit and receive state vary greatly. The coefficients were drawn into plots for each frequency and they are shown in Fig. 17. As this is experimental data, we do not have access to the true values.

The next step was to compute the calibrated scattered fields and the process was finalized by sending the data to CSI-FEM inversion. Grain permittivity of  $\Re(\epsilon)$  is shown in Fig. 9 for 260, 270, and 280 MHz, and  $\Re(\epsilon)$  is shown in Fig. 13 for 550, 560, and 570 MHz. We also show 3D threshold images in Figs. 11 and 15.

*Traditional Calibration:* In order to determine the quality of the single-shot calibrated images, we compare it to a traditional calibration approach. We thus applied traditional two data set calibration by generating the parametric fields

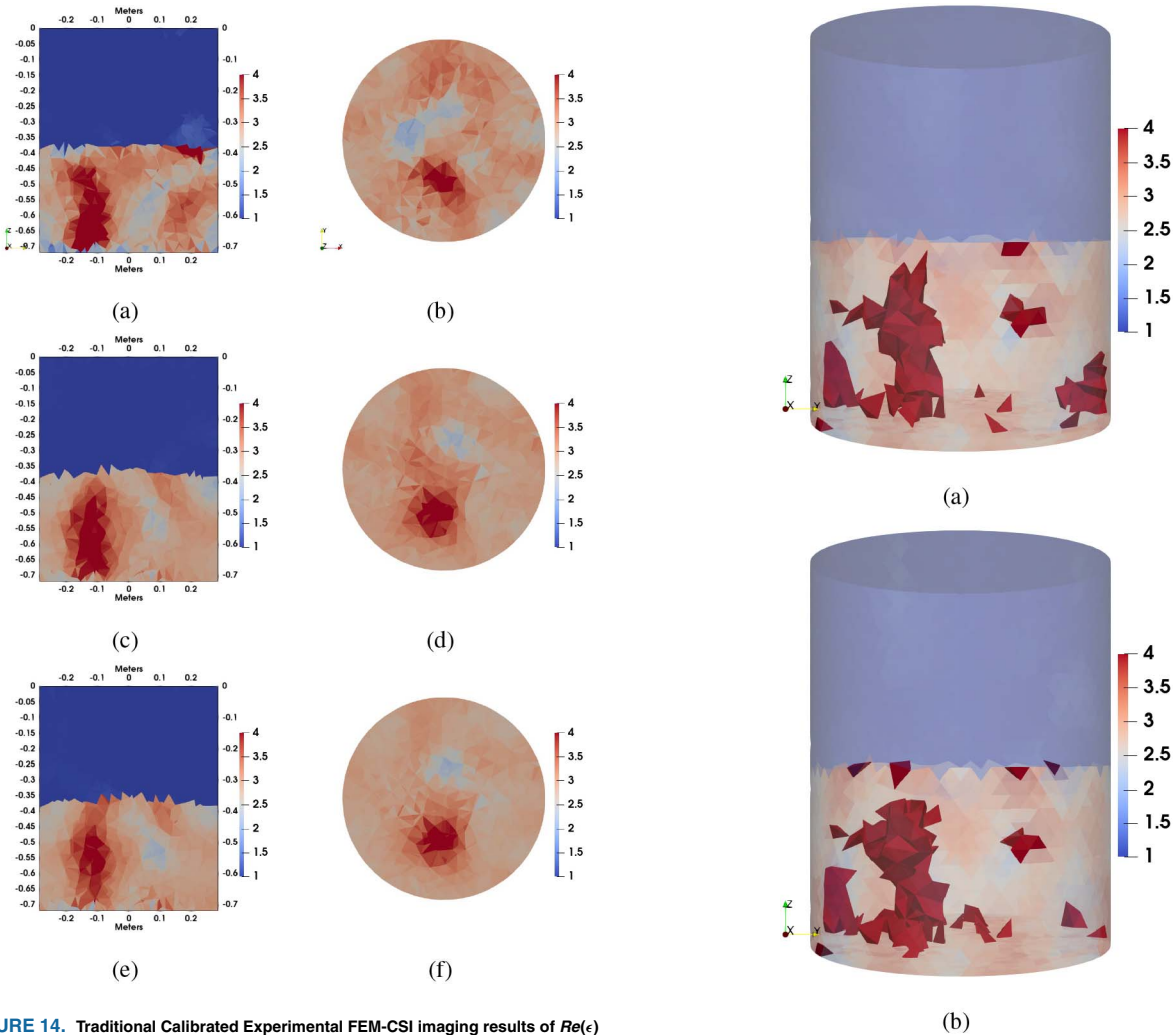


**FIGURE 14.** Traditional Calibrated Experimental FEM-CSI imaging results of  $Re(\epsilon)$  for the frequency band 500MHz. Standard calibration (a) vertical and (b) horizontal slice at 550MHz, (c) vertical and (d) horizontal slice at 560MHz, and (e) vertical and (f) horizontal slice at 570MHz.

associated with  $S_{xy}^{known}$ , and followed the calibration process outlined in (1). Other than changing the calibrated data, we keep all other parameters (meshes and stopping condition) of the FEM-CSI inversion were identical between the single-shot and traditional methods. The images associated with traditional calibration process are shown in Figs. 10 and 14. We have also presented 3D threshold images in Figs. 12 and 16.

*Single-shot work flow when no wet-grain target is present:* As a final experiment, we considered the case where we run the single-shot workflow on a data set collected where there is no wet-grain target present. That is,  $S_{xy}^{unknown}$  contains only homogeneous grain. For a frequency of 550 MHz, these results are shown in Fig. 18.

## VII. DISCUSSION

A careful comparison of the standard calibration and one-shot calibration images allows qualitative assessment of the proposed calibration technique. Overall, the single-shot images closely resemble the images obtained by applying



**FIGURE 15.** One-shot Calibrated Experimental FEM-CSI inversion 3D images of  $Re(\epsilon)$  with a threshold at the frequencies of (a) 550MHz, (b) 560MHz, and (c) 570MHz. All tetrahedrons beyond a threshold of 4 are solid.

the more standard calibration procedure, but have more image artifacts, particularly in the lower frequency band. Degradation in the one-shot calibrated images is most

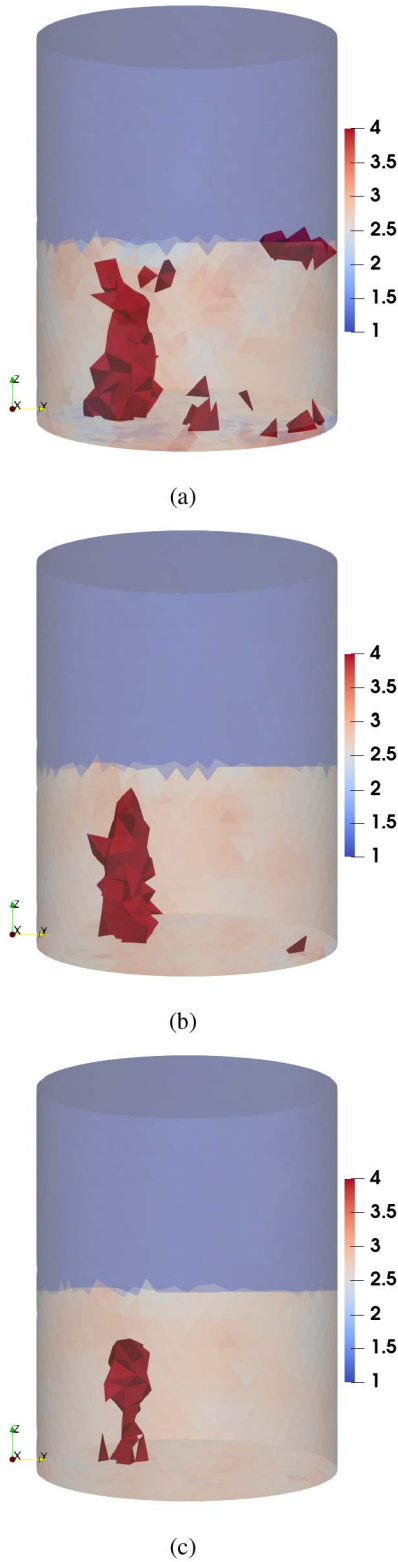


**FIGURE 16.** Traditional Calibrated Experimental FEM-CSI inversion 3D images of  $Re(\epsilon)$  with a threshold at the frequencies of (a) 550MHz, (b) 560MHz, and (c) 570MHz. All tetrahedrons beyond a threshold of 4 are solid.

clear in the 3D threshold images at the lower 250 MHz frequency band. We expect some degradation with one-shot as the traditional differential calibration procedure has

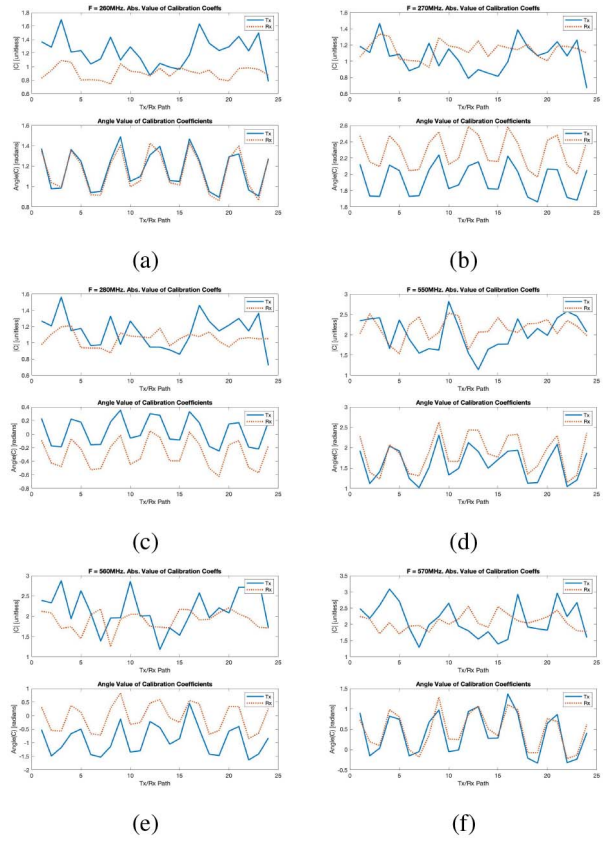


**FIGURE 17.** Calibration coefficient by transmit/receive path (or channel). (a) 260MHz (b) 270MHz (c) 280MHz (d) 550MHz (e) 560MHz (f) 570MHz. The coefficients in transmit mode are in blue (Tx), in receive mode are in red (Rx).

creates zero signal from anything that is common between the two measurements. Thus, there is no direct signal from any model imperfections (i.e., the physical barrel is different from the computational model), or the fact that the bulk grain may be homogeneous (whereas our initial model is homogeneous), etc. Our proposed one-shot calibration technique leads to signals that contain scattered field from all of these differences. These extra scattered fields mean the final images will not be as high quality when detecting a wet-grain target. An example of the image degradation we can expect is shown for the no-target case in Fig. 18.

In all images the hot-spot location is detectable, but the size of the hot-spot is larger at lower frequencies. This is expected as the target is quite small compared with the wavelength in the lower band (for example, wavelength of 260 MHz is 0.7 m, and the target dimensions are about 0.14 m maximum). It makes sense that the hot-spot is more distinguishable in the images with frequencies in the higher band due to the improved resolution available at higher frequencies. This is true for both one-shot and traditional calibration.

We also note that the cone angle in the standard calibration images appears to be different from the one-shot image. The explanation of this difference is that the parameters  $p$  are created with  $S^{known}$  for standard calibration whereas  $S^{unknown}$

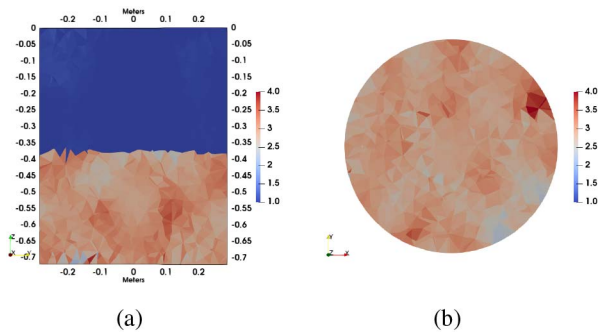


**FIGURE 18.** One-shot Calibrated Experimental FEM-CSI imaging results of  $Re(\epsilon)$  using the measurements with and without a wet-grain target for 550MHz. Without target (a) vertical and (b) horizontal slice. This image can be compared with Figs. 13(a) and (b), where the target was present.

is used for one-shot calibration. As the grain is homogeneous in  $S^{known}$ , and our parametric model assumes a homogeneous grain mass, this is a bias towards the traditional calibration providing more accurate images. While we could have used the parameters from  $S^{unknown}$  for the traditional calibration as well, we chose not to as we wanted to test the one-shot algorithm against the best case traditional calibration. Our results show that even with this bias, the proposed algorithm still performs comparably to the traditional case.

### VIII. CONCLUSION

We have proposed a one-shot calibration procedure that is capable of calibrating system errors and producing images with a single  $S$ -parameter data set. The net effect in grain bins is that we can image inhomogeneities with a single measurement in an uncooperative EMI system. In terms of practical benefit, grain handlers can now image inhomogeneous grain masses immediately after filling the bin.

In the proposed calibration method, we use per-channel and transmit/receive calibration coefficients and obtain estimates of these coefficients through optimization, combined with the use of a parametric inversion that provides estimates of the bulk contents of the bin. Synthetic and experimental results show that the procedure provides final images that are close, but slightly degraded compared to images from a two data-set calibration process. This degradation is acceptable as there is currently no other method for calibrating data in uncooperative imaging systems such as grain bins.

### REFERENCES

[1] S. O. Nelson, *Dielectric Properties of Agricultural Materials and Their Applications*. Cambridge, MA, USA: Academic Press, 2015, doi: 10.1016/C2014-0-02694-9. [Online]. Available: <https://www.sciencedirect.com/book/9780128023051/dielectric-properties-of-agricultural-materials-and-their-applications>

[2] J. LoVetri, M. A. Asefi, C. Gilmore, and I. Jeffrey, "Innovations in electromagnetic imaging technology: The stored-grain-monitoring case," *IEEE Antennas Propag. Mag.*, vol. 62, no. 5, pp. 33–42, Oct. 2020.

[3] M. Asefi, C. Gilmore, I. Jeffrey, J. LoVetri, and J. Paliwal, "Detection and continuous monitoring of localised high-moisture regions in a full-scale grain storage bin using electromagnetic imaging," *Biosyst. Eng.*, vol. 163, pp. 37–49, Nov. 2017.

[4] C. Gilmore, M. Asefi, J. Paliwal, and J. LoVetri, "Industrial scale electromagnetic grain bin monitoring," *Comput. Electron. Agricult.*, vol. 136, pp. 210–220, Apr. 2017.

[5] C. Gilmore, I. Jeffrey, M. Asefi, N. T. Geddert, K. G. Brown, and J. LoVetri, "Phaseless parametric inversion for system calibration and obtaining prior information," *IEEE Access*, vol. 7, pp. 128735–128745, 2019.

[6] K. Belkebir and M. Saillard, "Testing inversion algorithms against experimental data: Inhomogeneous targets," *Inverse Problems*, vol. 21, no. 6, p. S1, 2004.

[7] M. Ostadrahimi *et al.*, "Analysis of incident field modeling and incident/scattered field calibration techniques in microwave tomography," *IEEE Antennas Wireless Propag. Lett.*, vol. 10, pp. 900–903, 2011.

[8] M. Zimmermanns, I. Rolfes, M. Mallach, P. Gebhardt, and T. Musch, "Multiport calibration for microwave tomography systems," in *Proc. German Microwave Conf. (GeMiC)*, 2016, pp. 96–99.

[9] O. Karadima *et al.*, "Experimental validation of microwave tomography with the dbim-twist algorithm for brain stroke detection and classification," *Sensors*, vol. 20, no. 3, p. 840, 2020.

[10] D. O. Rodriguez-Duarte *et al.*, "Experimental validation of a microwave system for brain stroke 3-d imaging," *Diagnostics*, vol. 11, no. 7, p. 1232, 2021.

[11] M. Hopfer, R. Planas, A. Hamidipour, T. Henriksson, and S. Semenov, "Electromagnetic tomography for detection, differentiation, and monitoring of brain stroke: A virtual data and human head phantom study," *IEEE Antennas Propag. Mag.*, vol. 59, no. 5, pp. 86–97, Oct. 2017.

[12] C. Gilmore *et al.*, "A wideband microwave tomography system with a novel frequency selection procedure," *IEEE Trans. Biomed. Eng.*, vol. 57, no. 4, pp. 894–904, Apr. 2010.

[13] T. M. Grzegorzcyk, P. M. Meaney, P. A. Kaufman, R. M. Diflorio-Alexander, and K. D. Paulsen, "Fast 3-D tomographic microwave imaging for breast cancer detection," *IEEE Trans. Med. Imag.*, vol. 31, no. 8, pp. 1584–1592, Aug. 2012.

[14] J. A. T. Vasquez *et al.*, "A prototype microwave system for 3D brain stroke imaging," *Sensors*, vol. 20, no. 9, p. 2607, 2020.

[15] M. Asefi, G. Faucher, and J. LoVetri, "Surface-current measurements as data for electromagnetic imaging within metallic enclosures," *IEEE Trans. Microw. Theory Techn.*, vol. 64, no. 11, pp. 4039–4047, Nov. 2016.

[16] Z. Miao and P. Kosmas, "Multiple-frequency DBIM-TwIST algorithm for microwave breast imaging," *IEEE Trans. Antennas Propag.*, vol. 65, no. 5, pp. 2507–2516, May 2017.

[17] A. Baran, D. J. Kurrant, A. Zakaria, E. C. Fear, and J. LoVetri, "Breast imaging using microwave tomography with radar-based tissue-regions estimation," *Progress Electromagnetics Res.*, vol. 149, pp. 161–171, Oct. 2014.

[18] E. Kim, J. LoVetri, I. Jeffrey, and C. Gilmore, "Single data set calibration and imaging with uncooperative electromagnetic inversion systems," in *Proc. 15th Eur. Conf. Antennas Propag. (EuCAP)*, 2021, pp. 1–4.

[19] A. Zakaria, I. Jeffrey, J. LoVetri, and A. Zakaria, "Full-vectorial parallel finite-element contrast source inversion method," *Progress Electromagnetics Res.*, vol. 142, pp. 463–483, 2013.

[20] C. Gilmore, M. Asefi, K. Nemez, J. Paliwal, and J. LoVetri, "Three dimensional radio-frequency electromagnetic imaging of an in-bin grain conditioning process," *Comput. Electron. Agricult.*, vol. 167, Nov. 2019, Art. no. 105059.

[21] C. T. Mohadi, M. Asefi, and C. Gilmore, "Ferrite loaded shielded half loop antenna for electromagnetic imaging inside metallic chambers," in *Proc. 19th Int. Symp. Antenna Technol. Appl. Electromagnetics (ANTEM)*, 2021, pp. 1–3.

[22] K. Lawrence, S. Nelson, and P. Bartley, Jr., "Measuring dielectric properties of hard red winter wheat from 1 to 350 MHz with a flow-through coaxial sample holder," *Trans. ASAE*, vol. 41, no. 1, p. 143, 1998.